J. Fluid Mech. (2011), *vol.* 683, *pp.* 417–429. © Cambridge University Press 2011
doi:10.1017/jfm.2011.299

Flow visualization using reflective flakes

Susumu Goto[1]†, Shigeo Kida[2] and Shohei Fujiwara[3]

[1] Department of Mechanical Engineering, Okayama University, 3-1-1, Tsushima-naka, Kita, Okayama 700-8530, Japan

[2] Department of Mechanical Engineering, Doshisha University, 1-3, Tatara-miyakodani, Kyotanabe 610-0394, Japan

[3] Department of Mechanical Engineering and Science, Kyoto University, Yoshida-Honmachi, Sakyo, Kyoto 606-8501, Japan

(Received 7 March 2011; revised 3 May 2011; accepted 5 July 2011; first published online 18 August 2011)

The pattern in an image of flow visualizations using reflective flakes stems from their non-uniform orientation rather than their spatial accumulation. It is shown, based on the assumption that flakes are infinitely thin elliptic discs without inertia, that the temporal evolution of their orientations is identical to that for infinitesimal material surface elements. In general, bright regions in a visualized image are the superposition of those where the flake (i.e. the material surface element) orientation is isotropic and those where flakes tend to align in the direction for which the incident rays are reflected into the line of sight. A non-trivial example of the visualization of a steady flow in a precessing sphere is given to verify these conclusions.

Key words: general fluid mechanics, particle/fluid flows, turbulent mixing

1. Introduction

Flow visualization by reflective flakes has been widely used in laboratory experiments. For example, the Taylor vortices in the gap between two concentric rotating cylinders are clearly visualized by the use of reflective flakes; see e.g. the recent experiment by Abcha *et al.* (2008) as well as the album by Van Dyke (1982, pp. 76–77). Here, flakes are the small (the dimension is of the order of 10 μm and the thickness is as thin as 0.1 μm) flat plates as seen in their microscope image (figure 1). Since these flakes are reflective, visualized images reveal patterns according to their non-uniform orientations and/or their spatial accumulation, if any.

Although flake visualization is easy to conduct, it is generally difficult to answer the question of what kind of flow structures are visualized. This simple problem has been investigated by quite a few authors. For example, the frequently cited article of Savas (1985) concluded that 'thin flakes tend to align with stream surface'. However, the notion of the stream surface is defined only in two-dimensional flows, and the argument by Savas (1985) is limited to cases of parallel flows. Extensions to three-dimensional flow visualizations have been developed by several authors (Gauthier, Gondret & Rabaud 1998; Abcha *et al.* 2008; Hecht, Mucha & Turk 2010), but Gauthier *et al.* (1998) concluded that 'the legitimate question of what the visualization

† Email address for correspondence: goto@mech.okayama-u.ac.jp

https://doi.org/10.1017/jfm.2011.299 Published online by Cambridge University Press

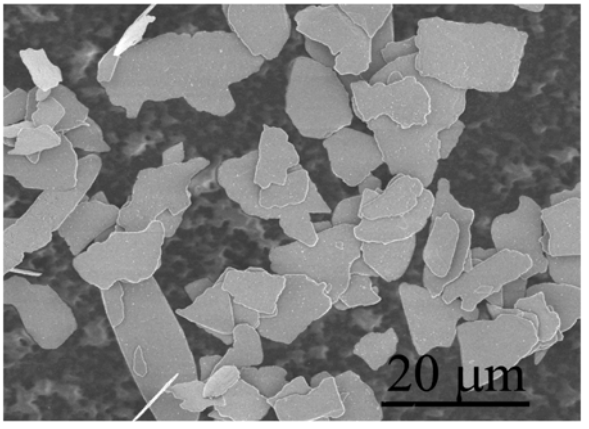


FIGURE 1. Microscope (scanning electron microscope) image of the reflective flakes (TiO_2-coated mica flakes for paints) used in our experiments. The dimension ranges between $\sim$10 μm and 40 μm, whereas the thickness is as thin as 0.1 μm.

shows does not have a simple answer', Abcha *et al.* (2008) treated specific cases of Taylor–Couette flows, and the argument by Hecht *et al.* (2010) is restricted to the case that the velocity gradient tensor is invariant on the flake orientation response time scale.

In the present article, we further investigate the visualization of three-dimensional flow using reflective flakes. Similarly to the previous studies (Savas 1985; Gauthier *et al.* 1998; Abcha *et al.* 2008; Hecht *et al.* 2010), our argument is based on the seminal work by Jeffery (1922), which derived the Stokes flow around an elliptic particle. As a related study, important contributions were made recently by Wilkinson, Bezuglyy & Mehlig (2009), Bezuglyy, Mehlig & Wilkinson (2010) and Wilkinson, Bezuglyy & Mehlig (2011). They derived the governing equation for an infinitely thin rod by regarding it as a dumbbell, and investigated the orientation of rods and flow visualizations by rodlike reflective particles in two-dimensional flows. As stated in Wilkinson *et al.* (2009), the equation for infinitely thin rods can be derived from the Jeffery equations; see also Szeri & Leal (1994) and Olbricht, Rallison & Leal (1982) for related studies. In the following, we apply their arguments to reflective flakes in three-dimensional flows. More concretely, we assume that the reflective flakes (figure 1) are infinitely thin elliptic discs without inertia, and this bold assumption leads to governing equations for reflective flakes that imply that flakes always distribute uniformly in space in an incompressible fluid, whereas the temporal evolution of their orientations is identical to that for infinitesimal material surface elements (§ 2). This conclusion is an extension of the treatment of thin rods in two-dimensional flows developed by Wilkinson and his coworkers. Note that the equation for thin rods implies that their angle evolution is identical to that of infinitesimal material line elements. Since there is no direct verification of the conclusion, it is worth verifying it experimentally by a non-trivial example (§ 3) so that it can serve as the basis to investigate the property of visualizations of three-dimensional flows using reflective flakes.

2. Governing equations for flakes

If the size of flakes is much smaller than the characteristic length of fluid motion, and the Stokes number is much less than unity, then the translational motion of a flake

https://doi.org/10.1017/jfm.2011.299 Published online by Cambridge University Press

is identical to that of the fluid particle at the same position, i.e.

$$\frac{\mathrm{d}\boldsymbol{x}}{\mathrm{d}t} = \boldsymbol{u}(\boldsymbol{x}(t), t), \tag{2.1}$$

where $\boldsymbol{x}(t)$ is the position vector of the flake at time t, and $\boldsymbol{u}(\boldsymbol{x}, t)$ denotes the fluid velocity at the position $\boldsymbol{x}$ and time t. We have also assumed that flakes are so diluted that interactions between them are negligible. Under these assumptions, the spatial distribution of flakes is always uniform in an incompressible fluid, if the initial distribution is so. In other words, this model cannot deal with the effects of flake accumulation.

As for the orientation of a flake, since the Reynolds number defined by the dimension of the flake and the relative velocity is negligibly small under the above assumption, its angular velocity $\boldsymbol{\Omega}$ can be expressed in terms of the gradients of fluid velocity $\boldsymbol{u}$ as follows. Jeffery (1922) derived the Stokes flow around an ellipsoidal particle whose shape is expressed by

$$\frac{x^2}{a_x^2} + \frac{y^2}{a_y^2} + \frac{z^2}{a_z^2} = 1 \tag{2.2}$$

in Cartesian coordinates (x, y, z). Here, a_x, a_y and a_z are constants. Then, he showed that its angular velocity $\boldsymbol{\Omega} = (\Omega_x, \Omega_y, \Omega_z)$ is expressed by

$$(a_y^2 + a_z^2)\Omega_x = a_y^2 \frac{\partial u_z}{\partial y} - a_z^2 \frac{\partial u_y}{\partial z}, \tag{2.3a}$$

$$(a_z^2 + a_x^2)\Omega_y = a_z^2 \frac{\partial u_x}{\partial z} - a_x^2 \frac{\partial u_z}{\partial x}, \tag{2.3b}$$

$$(a_x^2 + a_y^2)\Omega_z = a_x^2 \frac{\partial u_y}{\partial x} - a_y^2 \frac{\partial u_x}{\partial y}, \tag{2.3c}$$

when the moment of inertia of the ellipsoid is negligible. Since we have assumed that the shape of flakes is an infinitely thin elliptic disc, putting $a_z = 0$, from (2.3) we obtain

$$\Omega_x = \frac{\partial u_z}{\partial y}, \quad \Omega_y = -\frac{\partial u_z}{\partial x}, \quad \Omega_z = \frac{1}{1+\alpha}\frac{\partial u_y}{\partial x} - \frac{\alpha}{1+\alpha}\frac{\partial u_x}{\partial y}. \tag{2.4}$$

Here, we set the normal vector of the flake parallel to the z-axis, and α denotes a_y^2/a_x^2. Since the rotation around the z-axis does not change the orientation of the flake at all, we can put $\Omega_z = 0$. The angular velocity of the flake is, therefore, expressed by

$$\boldsymbol{\Omega} = -(\boldsymbol{n} \times \nabla)(\boldsymbol{n}\cdot\boldsymbol{u}), \tag{2.5}$$

where $\boldsymbol{n}$ is the normal vector of the flake. Thus, we obtain the governing equation for $\boldsymbol{n}$ as

$$\frac{\mathrm{d}\boldsymbol{n}}{\mathrm{d}t} = -(\boldsymbol{n} \times \nabla)(\boldsymbol{n}\cdot\boldsymbol{u}) \times \boldsymbol{n}. \tag{2.6}$$

Note that (2.6) is rewritten as

$$\frac{\mathrm{d}\boldsymbol{n}}{\mathrm{d}t} = -\nabla(\boldsymbol{n}\cdot\boldsymbol{u}) + \boldsymbol{n}[\boldsymbol{n}\cdot\nabla(\boldsymbol{n}\cdot\boldsymbol{u})], \tag{2.7}$$

and that the second term on the right-hand side of (2.7) has no contribution to the temporal change of the orientation of the flake, since it is parallel to $\boldsymbol{n}$.

https://doi.org/10.1017/jfm.2011.299 Published online by Cambridge University Press

(The term assures that the magnitude of $\boldsymbol{n}$ is constant in time.) Comparing (2.7) with the governing equation for an infinitesimal material surface element (see equation (3.1.5) in Batchelor (1967), for example) in incompressible fluids,

$$\frac{\mathrm{d}\boldsymbol{s}}{\mathrm{d}t} = -\boldsymbol{\nabla}(\boldsymbol{s}\cdot\boldsymbol{u}), \tag{2.8}$$

where $\boldsymbol{s}$ is the normal vector of a material surface element whose magnitude is proportional to its area, we realize that the temporal evolution of the normal vector of a flake is identical to that of an infinitesimal material surface element apart from the variation of the area in the latter. Hence, we can consider the behaviour of the orientation of material surface elements as that of flakes. The former is much easier to imagine because they are frozen in fluids. For example, since material surface elements are stretched by local strain, we may understand that they, and therefore flakes, can align into preferential directions (see figure 7*b*, below), which are determined by the integrated velocity gradients along their trajectory. This is a key property in the mechanism of flake visualizations, as seen in the next section.

Note that the treatment of the reflective flakes as material surface elements in three-dimensional flows is similar to the treatment of them as line elements in two-dimensional flows. The latter has been developed by Wilkinson *et al.* (2009), Bezuglyy *et al.* (2010) and Wilkinson *et al.* (2011). Though such a treatment is intuitive as well as justified theoretically based on the Jeffery equation (2.3), there is no experiment that supports it. We verify, therefore, the governing equations (2.1) and (2.6) experimentally in the next section.

3. Example

Here, we compare flake visualizations simulated numerically based on the governing equations (2.1) and (2.6) for flakes with visualizations in the laboratory to show that these equations describe the behaviour of flakes excellently.

For this purpose, we employ a steady flow in a precessing sphere (figure 2). The precession is the rotational motion of the axis (the horizontal axis in figure 2) of the spin at an angular velocity $\boldsymbol{\Omega}_s$ (where $\Omega_s = |\boldsymbol{\Omega}_s|$ is constant) around another axis (the precession axis, which is the vertical axis in the figure) at a constant angular velocity $\boldsymbol{\Omega}_p$. Incidentally, since the experiment by Malkus (1968) and the theoretical work by Busse (1968), flows inside a precessing cavity have been extensively studied mainly from the geophysical viewpoint because the Earth precesses weakly.

When the precession is weak (i.e. $\Omega_p \ll \Omega_s$), the flow in the precessing sphere is steady in the frame rotating at the angular velocity $\boldsymbol{\Omega}_p$. A global circulation approximately around the spin axis, which is inclined by the Coriolis force, is dominant in this steady flow; but since this nearly solid-body rotational flow is accompanied by a pair of conical shear layers, its flow structure is non-trivial. This steady flow is produced in both the laboratory experiment and the direct numerical simulation (DNS) under exactly the same conditions, and flake visualizations are conducted and simulated, respectively. More precisely, the Reynolds number defined by the magnitude Ω_s of the spin angular velocity, the radius a of the sphere and the kinematic viscosity ν of the fluid is fixed at

$$Re \equiv \frac{a^2\Omega_s}{\nu} = 80\,000, \tag{3.1}$$

https://doi.org/10.1017/jfm.2011.299 Published online by Cambridge University Press

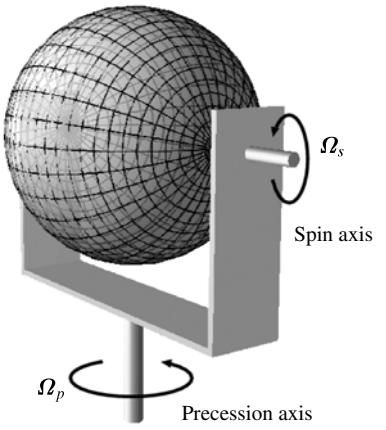


FIGURE 2. Precessing sphere. The spin axis of the spherical cavity rotates around the precession axis with a constant angular velocity $\boldsymbol{\Omega}_p$.

whereas the precession rate (the Poincaré number) is fixed at

$$\Gamma \equiv \frac{\Omega_p}{\Omega_s} = 0.002 \tag{3.2}$$

in both the experiment and DNS. Recall that the pair (Re, Γ) serve as complete control parameters of the current system.

3.1. *Experiment*

The laboratory experiment is conducted using the apparatus schematically depicted in figure 3. The sphere radius a is 90 mm. The light source for flow visualizations is a laser sheet (with a width of $\sim$1 mm), which runs through the centre of the sphere in the perpendicular direction to the spin axis. The incident laser beam along the precession axis is fanned out by a cylindrical lens located at $3.5a$ above the sphere centre. As shown in figure 3, we use an acrylic cylinder (refractive index 1.49) with a spherical cavity filled with water (refractive index 1.33). By refraction at the surfaces of the vessel, the incident rays become approximately parallel to the precession axis inside the cavity (figure 4). Light reflected by flakes is, then, recorded by a digital camera from the perspective along the spin axis. By using the cylindrical vessel, the distortion of the light reflected from the flakes as it leaves the sphere and enters the camera is minimized. Here, the flat window in the large bearing at the flat end of the cylinder plays a role.

Degassed water, in which a small amount (0.04 g for 3.05 kg of water, which is $\sim$13 ppm) of the flakes shown in figure 1 are seeded, is confined in the sphere. In order to control the Reynolds number precisely, we monitor the temperature of the water.

We start from rest, where the flake visualization is observed as a random pattern. First, only the spin at $Re = 80\,000$ is driven, and then the flow settles down to solid-body rotational flow around the spin axis. In this state, we observe a pale flake pattern (see the initial pattern of supplementary movie 2) probably because the flakes tend to align along the streamlines during the spin-up as demonstrated by Savas (1985). Then, we add the precession of $\Gamma = 0.002$, suddenly. After $\sim$50 periods of the spin, a beautiful steady pattern shown in figure 5(*a*) gradually appears (see also supplementary

https://doi.org/10.1017/jfm.2011.299 Published online by Cambridge University Press

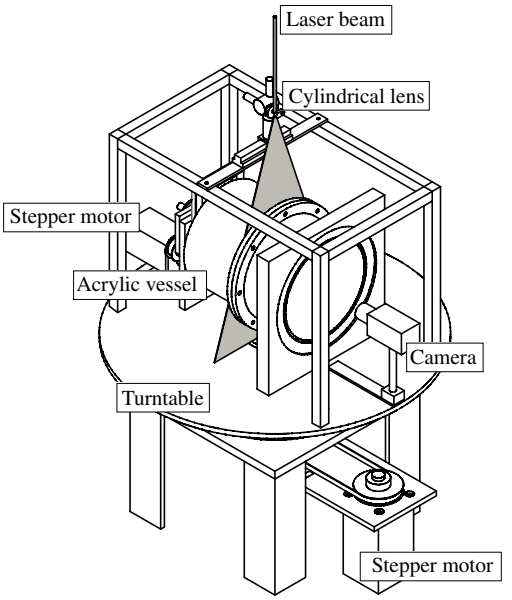


FIGURE 3. Experimental apparatus. The laser sheet runs through the centre of the sphere perpendicularly to the spin axis. The line of sight is along the spin axis. See supplementary movie 1 available at journals.cambridge.org/flm for the detailed drive mechanism.

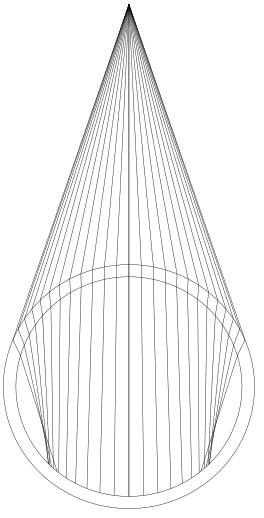


FIGURE 4. Orbits of incident rays numerically determined by taking into account the refractions on the surfaces of the acrylic vessel, the thickness of which is $0.11a$.

movie 2 for the temporal evolution). This pattern is robust and seems to be stationary for ever. We observe in the image subtle bright sector-shaped patterns in addition to three sharp approximately concentric circles. The radii of the circles, some parts of which are observed to be darker than the surrounding regions because of the property described in § 3.3 below, are measured by the use of the image of reference grids to be $\sim 0.38a$, $0.56a$ and $0.72a$. A similar pattern was observed also in a steady flow in a

https://doi.org/10.1017/jfm.2011.299 Published online by Cambridge University Press

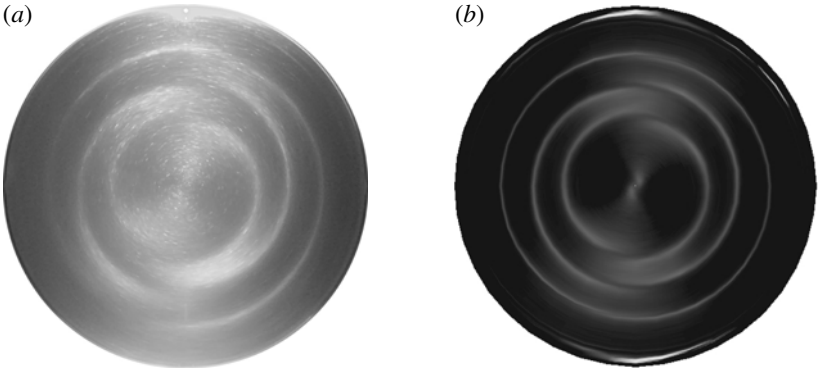


FIGURE 5. Flake visualization of the steady flow in a precessing sphere ($Re = 80\,000$ and $\Gamma = 0.002$). The incident rays are parallel to the precessing axis (which is vertical in the figure), and the perspective is along the spin axis (which is perpendicular to the page). (*a*) Laboratory experiment. See also the supplementary movie 2, which shows the temporal evolution of flake visualization for the duration of $200T_s$. (*b*) DNS. Flake motions are simulated by (2.1) and (2.6).

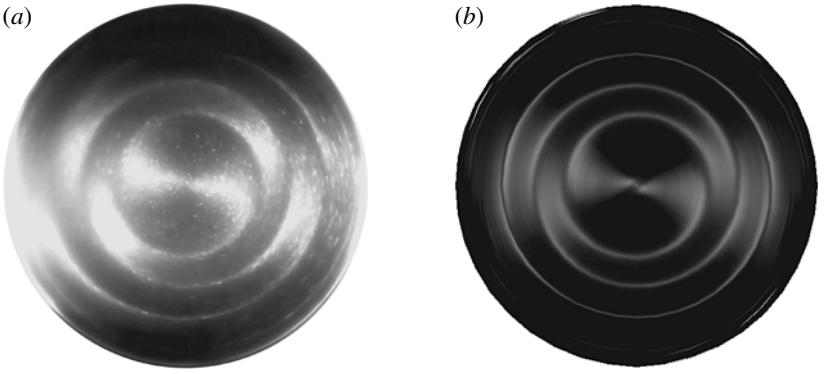


FIGURE 6. Same as figure 5 but the incident rays run from the right side of the figure. (*a*) Laboratory experiment. (*b*) DNS.

precessing spheroid (figure 7 in Vanyo *et al.* 1995). It is worth mentioning that we do not observe such a pattern when *spherical* particles with a size of ∼50 μm are laden instead of the flakes.

3.2. *Direct numerical simulation*

Steady flow at precisely the same Reynolds number Re and precession rate Γ is produced by DNS by the spectral method. Details of the numerical scheme are described in Kida & Nakayama (2008). The flake visualization in this steady flow is simulated under the assumption that the flake motions are governed by (2.1) and (2.6). The concrete procedure is summarized as follows.

(*a*) We choose, at time $t = 0$, inspection points uniformly on the plane of the visualization, i.e. the plane located at the centre of the sphere perpendicular to the spin axis.

https://doi.org/10.1017/jfm.2011.299 Published online by Cambridge University Press

(*b*) Starting from the individual point chosen in (*a*), we track backward in time the orbit of the flake (which is identical to the streamline in the steady flow) for the duration of 100 periods of the spin. More precisely, we integrate (2.1) from $t = 0$ to $t = -100T_s$ (where T_s is the spin period) by the fourth-order Runge–Kutta scheme with linear interpolation of the velocity field on sufficiently dense numerical grids to obtain the velocity on the orbits.

(*c*) We distribute 1000 flakes with an isotropic orientation at the end point of each orbit obtained in (*b*).

(*d*) We integrate (2.1) and (2.6) forward in time with the initial conditions prepared in (*c*) for the duration of $100T_s$. The velocity gradients on the orbits are linearly interpolated. Each orbit then returns to the position set in (*a*). Thus we obtain the orientation of the 1000 flakes at each inspection point on the visualization plane. (Examples of the angle distribution of normal vectors of flakes are shown in figure 7, below.)

(*e*) At each point on the visualized plane, the direction $\boldsymbol{i}$ of the incident rays is estimated numerically by taking into account their refraction at boundaries of the acrylic vessel. Since the line of sight is parallel to the spin axis, only when the normal vector $\boldsymbol{n}$ of a flake is in the bisectional direction $\boldsymbol{n}_0$ between $-\boldsymbol{i}$ and the spin axis is the reflected light observed. Therefore, we regard the number of flakes that satisfy the condition $|\boldsymbol{n}_0 \cdot \boldsymbol{n}| > c$ as the intensity of the observed light. The choice of threshold c is not trivial, but the qualitative feature of the visualized image is confirmed to be insensitive to c in the range $c \gtrsim 0.8$. So, here, we adopt $c = 0.9$.

The result thus obtained is shown in figure 5(*b*), which is almost identical to the laboratory visualization shown in figure 5(*a*), although the left-bottom region in (*a*) is darker than in (*b*) due to the finite extension of the laser sheet.

It may be worth mentioning, in passing, that the above procedure (*a*)–(*e*) is solely for efficient computation. If we were able to track a sufficiently large number of flakes in the sphere, we would obtain a similar result to figure 5(*b*) by monitoring the orientation of each flake crossing the visualization plane.

3.3. *Comparison*

The results (figure 5) of the experiment and the DNS are surprisingly similar to each other. The DNS reproduces not only the three bright concentric circles but also the subtle sector-shaped pattern in the regions between the circles. This result supports the validity of the assumption that we made in § 2. In other words, the intensity in the visualized images using reflective flakes is due to the non-uniform orientation of the flakes, and we can investigate flake orientations by the equation for infinitesimal material surface elements.

The excellent coincidence of the DNS and the laboratory experiment is observed also for the incident rays in a different direction. Figure 6(*a*) is the visualization in the laboratory, where the laser sheet runs in the perpendicular direction both to the spin and the precession axes (i.e. from the right side of the image). Note that we use another laser sheet for this experiment instead of the one shown in figures 3 and 4. The corresponding DNS result is shown in figure 6(*b*), which is quite similar to the experimental result.

It is interesting to observe the difference between the patterns in figures 5 and 6. The three sharp circles are observed in both images, but the pattern between the circles is rotated by a right angle. The origin of these similarities and differences is easily

https://doi.org/10.1017/jfm.2011.299 Published online by Cambridge University Press

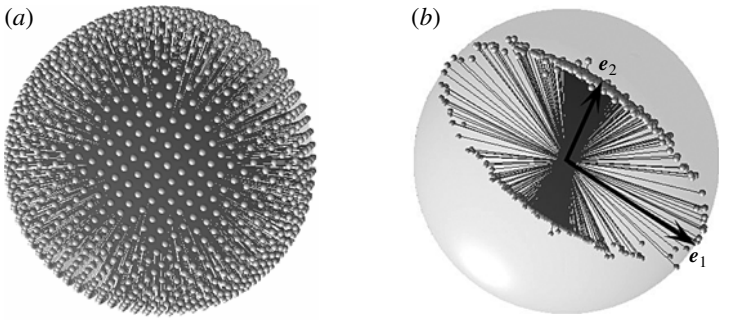


FIGURE 7. Angle distribution of the normal vectors of (1000) tracked flakes: (*a*) at a point on a bright circle (the radius of which is $\sim 0.38a$) in the visualization; (*b*) at a point (the distance of which from the centre is $\sim 0.76a$) off the bright circles. Arrows are eigenvectors $\boldsymbol{e}_1$ and $\boldsymbol{e}_2$ of $\boldsymbol{W}$.

seen by examining flake orientations. Figure 7 shows the angle distribution of unit normal vectors $\boldsymbol{n}$ of 1000 flakes tracked in DNS at two typical points: i.e. (*a*) at a point on a bright circle in figures 5 and 6, and (*b*) at a point off the bright circles. The former distribution is nearly isotropic, while a strong anisotropy is observed in the latter. In order to identify regions where the orientation of flakes is isotropic, we estimate the smallest eigenvalue λ of the second-order directional tensor defined by

$$T_{ij} = \langle n_i n_j \rangle. \tag{3.3}$$

Here, brackets $\langle\ \rangle$ denote the arithmetic average over the 1000 tracked flakes. The regions where λ is greater than a threshold (which is chosen to be 0.25 here) are plotted in figure 8. Recall that the trace of the symmetric tensor T_{ij} is unity because $|\boldsymbol{n}| = 1$, and that λ takes the maximum value $1/3$ if the orientation is precisely isotropic. Therefore, flake orientations in the shaded regions in the figure are nearly isotropic, and the regions are bright irrespective of the angles of incident rays and the line of sight because some of the flakes always reflect light to the observer. Figure 8 shows that such an isotropic orientation is established always and only (except in the vicinity of the centre) around three circles, and that their radii ($\sim 0.38a$, $0.56a$ and $0.72a$) coincide with those of the bright circles in figures 5 and 6. On the contrary, in the regions off the circles, where the minimum eigenvalue λ of T_{ij} takes small values, the orientation is anisotropic. More precisely, the angle distribution at points off the circles tends to be two-dimensional (as shown in figure 7*b*). This is consistent with the observation that the probability density function of λ has a keen peak at the origin (figure is omitted). Therefore, such regions are bright only when the angles of incident rays and the line of sight are appropriate for the flakes to reflect light to the observer.

The cause of the two different angle distributions (figure 7) is explained as follows. As shown in § 2, the temporal evolution of the flake normals $\boldsymbol{n}$ is identical to that of the infinitesimal material surface elements $\boldsymbol{s}$, which are governed by the linear equation (2.8). Recall that the precession of the present system is very weak ($\Gamma = 0.002$), and a solid-body rotational flow is dominant. The trajectory of a flake is, therefore, approximately closed. So the Poincaré map of $\boldsymbol{s}$ can be defined; that is, since (2.8) is linear, the temporal evolution of $\boldsymbol{s}$ is described by a linear map as $\boldsymbol{s}^{(i+1)} = \boldsymbol{W}\boldsymbol{s}^{(i)}$, where $\boldsymbol{s}^{(i)}$ denotes $\boldsymbol{s}$ for the surface element that passes through the visualization plane for the ith time. Thus, the temporal evolution of the angle

https://doi.org/10.1017/jfm.2011.299 Published online by Cambridge University Press

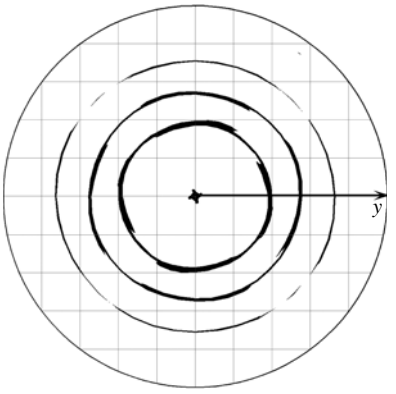


FIGURE 8. Regions where the orientation of flakes is nearly isotropic. The grid width indicates $0.2a$.

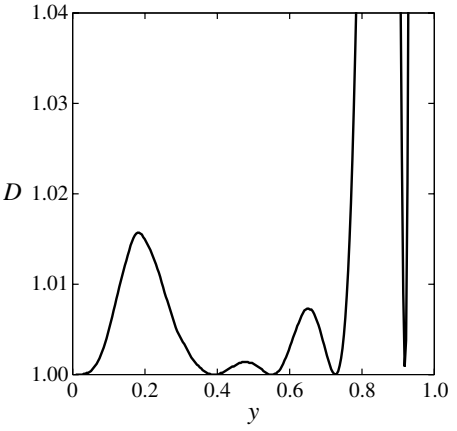


FIGURE 9. Index D, defined by (3.4), of change of the angles between flake normals. Horizontal axis is the y-axis shown in figure 8.

distribution of flake normals $\boldsymbol{n} = \boldsymbol{s}/|\boldsymbol{s}|$ is described by the matrix $\boldsymbol{W}$, which is the integral of velocity gradients along the flake trajectory.

Let D be

$$D = w_1 w_2 w_3/|\boldsymbol{W}|, \tag{3.4}$$

where w_j is the magnitude of the jth column vector of $\boldsymbol{W}$, and $|\boldsymbol{W}|$ is the determinant of $\boldsymbol{W}$. Note that if $D = 1$, $\boldsymbol{W}$ preserves the angles between the three orthogonal flake normals. In other words, for points with $D = 1$, the contributions of velocity gradients cancel out, and the angle distribution does not change by the effect of the internal shear. Therefore, for such a point, the distribution becomes isotropic eventually owing to the thermal fluctuations, even if the initial distribution is anisotropic. According to Savas (1985), the time scale of thermal motions is $\sim$100 s ($\approx$160 spin periods in the present case) for flakes in water. Indeed, it is numerically verified in figure 9 that $D = 1$ only on the three bright concentric circles, where the angle distribution is isotropic (figure 8).

https://doi.org/10.1017/jfm.2011.299 Published online by Cambridge University Press

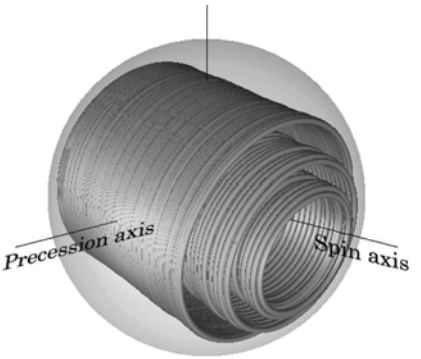


FIGURE 10. Orbits of flakes whose angle distribution is isotropic.

However, for points with $D > 1$, the angle distribution changes due to the shear layer on the flake trajectory. The preferable orientations of flake normals are determined by the eigenvectors of $\boldsymbol{W}$. For example, in the case shown in figure 7(*b*), the eigenvalues of $\boldsymbol{W}$ are 1.001 and $0.9991 \pm 0.0433\mathrm{i}$. Therefore, denoting the corresponding eigenvectors by $\boldsymbol{e}_1$ and $\boldsymbol{e}_2 \pm \mathrm{i}\boldsymbol{e}_3$ (where $|\boldsymbol{e}_3|/|\boldsymbol{e}_2| \approx 0.15$), the normals accumulate on the plane spanned by $\boldsymbol{e}_1$ and $\boldsymbol{e}_2$ after dozens of revolutions. This is confirmed in figure 7(*b*), where $\boldsymbol{e}_1$ and $\boldsymbol{e}_2$ are shown by arrows. The time scale of the accumulation estimated by the eigenvalues is also consistent with the observation ($\sim$50 spin periods, see supplementary movie 2). Since the internal shear is weak, the eigenvalues are approximately unity, and therefore such a two-dimensional distribution as shown in figure 7(*b*) is persistent for $O(10^4)$ revolutions before it eventually converges to $\boldsymbol{e}_1$. Note that this convergence cannot occur in practice because, before such a long time, the assumption of the closed trajectory is violated, and also thermal randomization takes place.

It is further interesting to investigate the three-dimensional structure where the angle distribution of flakes is isotropic, since such regions are always bright in flake visualizations. Figure 10 is such a structure numerically identified by the similar method as in figure 8. Since the structure is triple concentric cylinders, when the incident rays run on the plane spanned by the spin and precession axes, approximately parallel bright stripes are expected to be observed. This is verified in our experiment (figure is omitted, but a similar flake visualization of the flow in a precessing spheroid is given in figure 7 in Cardin & Olson (2007), where inclined parallel light bands are observed clearly).

4. Conclusion

Based on the above observations, we conclude the following. (i) The light intensity in an image of flake visualizations stems from the non-uniform orientations, rather than the non-uniform spatial distribution, of flakes. (ii) The temporal evolution of the orientation of a flake is well described by (2.6), which implies that the evolution is identical to that of an infinitesimal material surface element. (iii) There are, in general, two kinds of regions, where the orientation of flakes is isotropic or anisotropic, and the former regions are always bright in a visualized image irrespective of the angles of incident rays and the line of sight, while the intensity of the latter regions depends on them. In the present system, where flake trajectories are approximately closed, these

https://doi.org/10.1017/jfm.2011.299 Published online by Cambridge University Press

two regions are distinguished by the feature of the Poincaré map matrix $\boldsymbol{W}$ of material surface elements.

These conclusions may lead to some discussions on flow visualizations using reflective flakes. First, conclusions (i) and (ii) imply that bright regions of an image are those where the normal vectors of material surface elements, which spend sufficiently long time in the fluid, are in the bisectional directions between the incident rays and the line of sight. However, the orientation of material surface elements (and flakes) can be predicted only in simple cases such as steady parallel flows, where the velocity gradients are invariant along streamlines. For example, it is easily shown that the most probable alignment of material surface elements (and flakes) in a simple shear flow, after a duration sufficiently longer than the characteristic time scale of the shear rate, is in the direction of streamlines. This is consistent with the conclusion of Savas (1985). Note also that the orientation of a flake depends on its initial condition and history. For example, it is obvious that the visualized pattern depends on the initial orientation in a solid-body rotational flow, since the orientations are preserved. Secondly, conclusion (iii) means that two completely different regions coexist in bright regions of a visualized image. In the example considered in § 3, the three sharp concentric circles have the special property that flakes are distributed isotropically. In order to distinguish these circles from the other bright parts in the image, we must use multiple or multiple incident rays. Indeed, Thoroddsen & Bauer (1999) proposed a technique of flow visualization using reflective flakes together with multiple (and different-coloured) lights, and it was applied to surface visualization of a stirred suspension of reflective particles (Bezuglyy *et al.* 2010).

Before closing this article, it may be worth mentioning flake visualizations of turbulent flows. Note that the governing equations for flakes are valid for turbulent flows provided that the flake size ($\approx 10^{-5}$ m for flakes shown in figure 1) is much smaller than the Kolmogorov length, and the Stokes time ($\approx 10^{-4}$ s) is much smaller than the Kolmogorov time. Since the theoretical work by Batchelor (1952), the behaviour of infinitesimal material surface elements in turbulence has been extensively investigated (see e.g. Goto & Kida 2007 and references therein). Because the evolution of the orientation of material surface elements is governed by the smallest-scale (i.e. the Kolmogorov length, η) vortices, the characteristic length of the pattern in a visualization corresponds to the Kolmogorov length, if a sufficiently thin light sheet (which must not be thicker than the radius, $\sim 5\eta$, of the smallest coherent vortex tubes) is used. Therefore, as expected intuitively, the complexity of the pattern in a visualization may well reflect the development of turbulence. However, it has been shown by Girimaji & Pope (1990) that there is no direct correspondence between the surface element orientation and the eigenvectors of the strain tensor or the vorticity vector. Therefore, even if we can identify, by the use of multiple lights, for example, the orientation of flakes at each location, it is not possible to identify the velocity gradients. Nevertheless, since the coherent vortex tubes have life much longer than the Kolmogorov time (which is the time scale of the evolution of flake orientation), we may expect some correspondence between the intensity in a visualized image and coherent structures, as claimed experimentally by Schwarz (1990). Numerical verification of this prediction might be an interesting near-future study.

The authors would like to express their gratitude to Dr T. Tsukahara and Professor G. Kawahara for discussions. This work was supported by a Grant-in-Aid for Young

https://doi.org/10.1017/jfm.2011.299 Published online by Cambridge University Press

Scientists (21760130). The DNS were performed under the auspices of the NIFS Collaboration Research Program (NIFS08KTBL006).

Supplementary movies are available at journals.cambridge.org/flm.

REFERENCES

ABCHA, N., LATRACHE, N., DUMOUCHEL, F. & MUTABAZI, I. 2008 Qualitative relation between reflected light intensity by kalliroscope flakes and velocity field in the Couette–Taylor system. *Exp. Fluids* **45**, 85–94.

BATCHELOR, G. K. 1952 The effect of homogeneous turbulence on material lines and surfaces. *Proc. R. Soc. Lond.* A **213**, 349–366.

BATCHELOR, G. K. 1967 *An Introduction to Fluid Dynamics*. Cambridge University Press.

BEZUGLYY, V., MEHLIG, B. & WILKINSON, M. 2010 Poincaré indices of rheoscopic visualisations. *Europhys. Lett.* **89**, 34003.

BUSSE, F. H. 1968 Steady fluid flow in a precessing spheroidal shell. *J. Fluid Mech.* **33**, 739–751.

CARDIN, P. & OLSON, P. 2007 Experiment on core dynamics. In *Core Dynamics of Treatise on Geophysics* (ed. G. Schubert). vol. 8. pp. 319–345. Elsevier.

GAUTHIER, G., GONDRET, P. & RABAUD, M. 1998 Motions of anisotropic particles: application to visualization of three-dimensional flows. *Phys. Fluids* **10**, 2147–2154.

GIRIMAJI, S. S. & POPE, S. B. 1990 Material-element deformation in isotropic turbulence. *J. Fluid Mech.* **220**, 427–458.

GOTO, S. & KIDA, S. 2007 Reynolds-number dependence of line and surface stretching in turbulence: folding effects. *J. Fluid Mech.* **586**, 59–81.

HECHT, F., MUCHA, P. J. & TURK, G. 2010 Virtual rheoscopic fluids. *IEEE Trans. Vis. Comput. Graphics* **16**, 147–160.

JEFFERY, G. B. 1922 The motion of ellipsoidal particles immersed in a viscous fluid. *Proc. R. Soc. Lond.* A **102**, 161–179.

KIDA, S. & NAKAYAMA, K. 2008 Helical flow structure in a precessing sphere. *J. Phys. Soc. Japan* **77**, 05441.

MALKUS, W. V. R. 1968 Precession of the Earth as the cause of geomagnetism. *Science* **160**, 259–264.

OLBRICHT, W., RALLISON, J. M. & LEAL, L. G. 1982 Strong flow criteria based on microstructure deformation. *J. Non-Newtonian Fluid Mech.* **10**, 291–318.

SAVAS, Ö 1985 On flow visualization using reflective flakes. *J. Fluid Mech.* **152**, 235–248.

SCHWARZ, K. W. 1990 Evidence for organized small-scale structure in fully developed turbulence. *Phys. Rev. Lett.* **64**, 415–418.

SZERI, A. J. & LEAL, L. G. 1994 Orientation dynamics and stretching particles in unsteady, three-dimensional fliud flows: unsteady attractors. *Chaos, Solitons Fractals* **4**, 913–927.

THORODDSEN, S. T. & BAUER, J. M. 1999 Qualitative flow visualization using colored lights and reflective flakes. *Phys. Fluids* **11**, 1702–1704.

VAN DYKE, M. 1982 *An Album of Fluid Motion*. Parabolic Press.

VANYO, J., WILDE, P., CARDIN, P. & OLSON, P. 1995 Experiments on precessing flows in the earth's liquid core. *Geophys. J. Intl* **121**, 136–142.

WILKINSON, M., BEZUGLYY, V. & MEHLIG, B. 2009 Fingerprints of random flows? *Phys. Fluids* **21**, 043304.

WILKINSON, M., BEZUGLYY, V. & MEHLIG, B. 2011 Emergent order in rheoscopic swirls. *J. Fluid Mech.* **667**, 158–187.

https://doi.org/10.1017/jfm.2011.299 Published online by Cambridge University Press